



HAL
open science

Statistics of rogue waves in isotropic wave fields

Guillaume Michel, Félicien Bonnefoy, Guillaume Ducrozet, Eric Falcon

► **To cite this version:**

Guillaume Michel, Félicien Bonnefoy, Guillaume Ducrozet, Eric Falcon. Statistics of rogue waves in isotropic wave fields. *Journal of Fluid Mechanics*, 2022, 943 (A26), 10.1017/jfm.2022.436 . hal-03694182

HAL Id: hal-03694182

<https://hal.science/hal-03694182>

Submitted on 13 Jun 2022

HAL is a multi-disciplinary open access archive for the deposit and dissemination of scientific research documents, whether they are published or not. The documents may come from teaching and research institutions in France or abroad, or from public or private research centers.

L'archive ouverte pluridisciplinaire **HAL**, est destinée au dépôt et à la diffusion de documents scientifiques de niveau recherche, publiés ou non, émanant des établissements d'enseignement et de recherche français ou étrangers, des laboratoires publics ou privés.



Distributed under a Creative Commons Attribution - NonCommercial 4.0 International License

Banner appropriate to article type will appear here in typeset article

1 **Statistics of rogue waves in isotropic wave fields**

2 **Guillaume Michel¹†, Félicien Bonnefoy², Guillaume Ducroz² and Eric Falcon³**

3 ¹Sorbonne Université, CNRS, Institut Jean Le Rond d'Alembert, F-75005 Paris, France

4 ²École Centrale de Nantes, LHEEA, UMR 6598 CNRS, F-44321 Nantes, France

5 ³Université Paris Cité, CNRS, MSC, UMR 7057, F-75013 Paris, France

6 (Received xx; revised xx; accepted xx)

7 We investigate the statistics of rogue waves occurring in the inverse cascade of surface gravity
8 wave turbulence. In such statistically homogeneous, stationary and isotropic wave fields, low-
9 frequency waves are generated by nonlinear interactions rather than directly forced by a wave
10 maker. This provides a laboratory realization of arguably the simplest nonlinear sea state,
11 in which long-time acquisitions are performed and compared with theoretical models. The
12 analysis of thousands of rogue waves reveals that some of their properties crucially depend
13 on four-wave resonant interactions, large crests being for instance more likely than predicted
14 by second-order models.

15 **1. Introduction**

16 As a result of cheaper computational storage and improved sensors, the number of surface
17 waves included in databases of field measurements has soared over recent decades, going
18 from fifty thousand at the end of the 1970s to hundreds of millions in 2020 (Forristall
19 1978; Karpadakis *et al.* 2020). They allow for systematic correlation studies with hindcast
20 data, evidencing, for instance, that the probability of occurrence of rogue waves (RWs)
21 is independent of the instantaneous wind speed and direction (Christou & Ewans 2014).
22 These approaches are undoubtedly valuable as they single out the environmental conditions
23 that favour the occurrence of RW but remain far from being exhaustive. For instance, the
24 overwhelming majority of deep-water waves discussed in this context in Christou & Ewans
25 (2014) share the same directions of swell and current, precluding the possible evidence
26 of generation of RW by wave-current interactions, a phenomenon yet recognized as a
27 promising outlook (Adcock & Taylor 2014; Toffoli *et al.* 2015; Ducroz *et al.* 2021).
28 More fundamentally, drawing a comprehensive theory of RWs based on these results is
29 complicated by the lack of statistically stationary states: in practice, wave elevation time
30 series from different storms are spliced into 20 min samples then recombined with others
31 sharing similar proxies (e.g., wave mean frequency, mean direction of propagation, etc.),
32 which unavoidably introduces a bias and explains why the distribution of rare events such as
33 RWs is still discussed.

34 To assess theoretical models, laboratory experiments nicely complement field experiments
35 since they provide long-time statistics under controlled conditions. Most of them take place
36 in long flumes in which *unidirectional* waves, also referred to as “long-crested waves”, are

† Email address for correspondence: guillaume.michel@upmc.fr

37 randomly generated by a wave maker and propagate over more than a hundred meter before
 38 being damped by a beach. Such experiments typically report a transient overshoot of the
 39 kurtosis, of the spectral width and of the RW probability associated with the emergence of
 40 high-amplitude structures locally akin to the so-called Peregrine soliton (PS) (Onorato *et al.*
 41 2004, 2005, 2006; Shemer & Sergeeva 2009; Shemer *et al.* 2010*b,a*; Cazaubiel *et al.* 2018;
 42 Dematteis *et al.* 2019; Michel *et al.* 2020). This dynamics can be modelled by the nonlinear
 43 Schrödinger equation (NLSE), an exact solution of the latter, localized in both space and time,
 44 being the PS. The instability of a continuous wave train, called the “modulation instability”
 45 and generating RWs, can also be studied in long one-dimensional flumes and described by
 46 the NLSE, see, e.g., Lighthill (1965); Benjamin & Feir (1967); Lake *et al.* (1977); Melville
 47 (1982); Chabchoub *et al.* (2017) and references therein. All these results strongly depend
 48 on the directionality of the wave field, as shown both theoretically through the existence
 49 of transverse instabilities (Badulin & Ivonin 2012; Ablowitz & Cole 2021), numerically
 50 (Onorato *et al.* 2002; Soquet-Juglard *et al.* 2005; Gramstad & Trulsen 2007; Toffoli *et al.*
 51 2008) and experimentally (Waseda 2006; Onorato *et al.* 2009), questioning their relevance
 52 in accounting for *in situ* RWs.

53 On the other hand, another set of experiments investigate the theory of weak wave
 54 turbulence (WWT), which predicts how energy spreads among random waves in nonlinear
 55 interaction (Falcon & Mordant 2022). They take place in basins with reflecting walls and
 56 deal with *isotropic* or at least strongly multidirectional waves (“short-crested waves”). Until
 57 recently, they essentially consisted of generating waves with a wavelength a fraction of the
 58 length of the basin and measuring the energy cascade toward small scales (Denissenko *et al.*
 59 2007; Lukaschuk *et al.* 2009; Nazarenko *et al.* 2010; Deike *et al.* 2015; Aubourg *et al.* 2017;
 60 Campagne *et al.* 2018). A breakthrough occurred in 2020, when it was evidenced that forcing
 61 multidirectional random waves of short wavelengths in such basins not only generates even
 62 shorter wavelengths but also larger ones, corresponding to the inverse cascade of WWT
 63 (Falcon *et al.* 2020). Such wave fields are valuable for the study of RWs since the waves
 64 involved in their dynamics are spontaneously generated by nonlinear interactions rather
 65 than directly forced by the wave-maker. Moreover, they verify isotropy, homogeneity and
 66 stationarity, and therefore offer a unique framework to confront theoretical predictions on
 67 RWs to a simplified though strongly nonlinear model of the sea state. The present study
 68 reports the statistics of thousands of RWs measured in such a state and investigates the effect
 69 of high-order nonlinearities.

70 2. Experimental setup

71 Experiments are carried out in the large-scale basin (40 m long \times 30 m wide \times 5 m
 72 deep) of Ecole Centrale de Nantes, France. At one end of the basin, 48 flaps of width
 73 $\ell = 0.62$ m are driven independently by different realizations of white noise filtered in the
 74 $[f_0 - \Delta f, f_0 + \Delta f]$ frequency range, with $f_0 = 1.8$ Hz the central frequency and $\Delta f = 0.2$ Hz
 75 the bandwidth. Therefore, each flap generates independent waves of frequency around f_0
 76 (wavelength $\lambda_0 = 0.48$ m, group velocity $v_g = 0.43$ m \cdot s $^{-1}$) with a directional spread that
 77 can be estimated as $\theta = 2 \times (\lambda_0/\ell) = 88^\circ$. Three forcing amplitudes are considered, hereafter
 78 referred to, in increasing order, as Runs 1 to 3. At the other end, a solid vertical wall is built
 79 ahead of the usual beach. This setup is sketched in Fig. 1 Left.

80 As reported in Falcon *et al.* (2020), a statistically stationary, homogeneous and isotropic
 81 nonlinear steady state is reached after a transient of up to twenty minutes. The general
 82 picture is as follows: during this transient, the waves generated at f_0 by the flaps travel over
 83 nearly 70 times the length of the basin (20 min/ $v_g = 2.8$ km). As they propagate, nonlinear
 84 effects such as four-wave resonant interactions and very steep structures spread energy in all

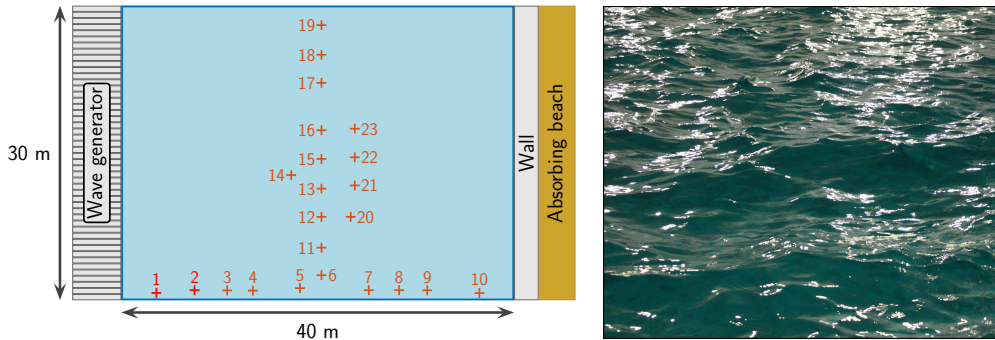


Figure 1: Left: Experimental setup showing the 48 flap wave generator, the end wall and the 23 probes. Probes 1 and 2 are used to verify the wave maker behaviour and are not included in the data analysis. Right: Photograph of a typical wave field (Run 3, the horizontal field of view is approximately one metre).

85 directions. Some of these strongly nonlinear effects visible from the shore are found to occur
 86 homogeneously in the basin, e.g. capillary waves generated by large gravity waves. Note that
 87 white capping is not observed, see Fig. 1 Right.

88 The surface elevations $\{\eta_i(t)\}_{i=1\dots 23}$ are recorded by 23 resistive probes of vertical
 89 resolution 0.1 mm and frequency resolution 100 Hz during 27 to 30 hours depending on the
 90 run. These measurements can be used to verify the claims of stationarity, homogeneity and
 91 isotropy. Stationarity is confirmed through the time evolution of statistical measurements of
 92 the wave field, e.g. the standard deviation of surface elevations computed over one minute
 93 samples, and is achieved after up to twenty minutes, see figures in Falcon *et al.* (2020). The
 94 transients are not investigated in this study and only measurements performed in the steady-
 95 state regimes are hereafter discussed. All probes are found to measure a similar standard
 96 deviation of surface elevation up to a maximum relative difference of 10%: homogeneity is
 97 closely achieved, and to remove the small remaining bias each signal is normalized by the
 98 standard deviation of the corresponding probe. Isotropy is the most challenging assumption
 99 to test since it cannot be investigated from a single elevation signal. The cross-correlation
 100 between pairs of elevation signals is therefore introduced. For each run, it is computed as

$$101 \quad R_{i,j}(\tau) = \frac{\langle \eta_i(t) \eta_j(t + \tau) \rangle}{\sqrt{\langle \eta_i(t)^2 \rangle \langle \eta_j(t)^2 \rangle}}, \quad (2.1)$$

102 where $\langle \cdot \rangle$ denotes a temporal averaging. Over all runs, all lags τ and all probes $i \neq j$, $|R_{i,j}|$
 103 remains less than 0.2 and the probes are therefore largely uncorrelated, as expected from
 104 their large spatial separation. Nevertheless, the remaining correlations evidence that $R_{i,j}(\tau)$
 105 is almost symmetric, i.e. that the wave field is essentially isotropic ($R_{i,j}(|\tau|)$ and $R_{i,j}(-|\tau|)$,
 106 respectively, account for signals propagating from i to j and from j to i). Quantitatively,
 107 with $(i \neq j) \in [13, 14, 15]$ standing for the three close central probes and τ_{\max} such that
 108 $R_{i,j}(\tau_{\max})$ is maximum,

$$109 \quad \left| \frac{R_{i,j}(\tau_{\max}) - R_{i,j}(-\tau_{\max})}{R_{i,j}(\tau_{\max})} \right| < 0.16, \quad (2.2)$$

110 a strong indication toward isotropy. Finally, note that the power spectrum density $S_\eta(f)$
 111 (PSD), reported in Fig. 2, reveals that most of the energy is located at frequencies *smaller*
 112 *than* the forcing range, corresponding to waves forced by nonlinear interactions. These PSDs

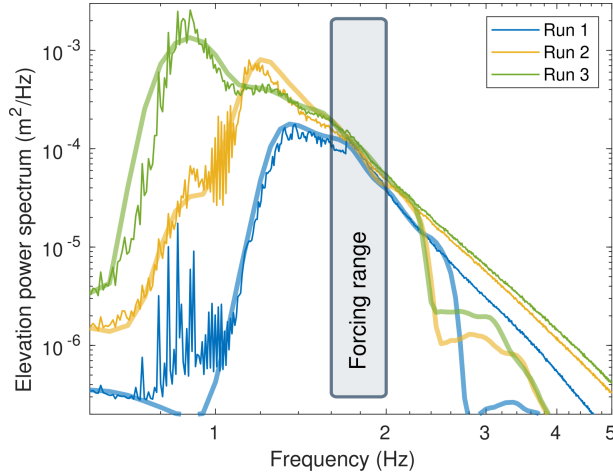


Figure 2: PSD of surface elevation for the three different steady states considered. Thin lines correspond to experimental results and thick ones to their numerical model. The forcing bandwidth is also displayed.

113 present some features theoretically predicted for the inverse cascade of WWT and derived
 114 under the assumption of stationarity, homogeneity and isotropy (Falcon *et al.* 2020).

115 It is instructive to detail the energy budget of this wave field. Energy is injected in the wave
 116 system at a rate \mathcal{P}_{inj} that can be measured through decay experiments and is of several watts
 117 (see Falcon *et al.* (2020), note that this power is much smaller than the one supplied to the
 118 wave maker). Conversely, the power dissipated by viscosity at high frequency ($> 2\text{Hz}$) at the
 119 surface boundary layer can be estimated from the experimental PSD and reads (Miles 1967)

$$120 \quad \mathcal{P}_{\text{diss}} = 2S\rho g \int_{2\text{Hz}}^{\infty} S_{\eta}(f)\alpha(f)df, \quad (2.3)$$

121 with $S = 30 \times 40 \text{ m}^2$ the surface of the basin, $\rho = 10^3 \text{ kg} \cdot \text{m}^{-3}$ the density, $g = 9.81 \text{ m} \cdot \text{s}^{-2}$
 122 the acceleration due to gravity, $\alpha(f) = 2\nu k^2 = 2\nu(2\pi f)^4/g^2$ the damping coefficient for
 123 clean water and $\nu = 10^{-6} \text{ m}^2 \cdot \text{s}^{-1}$ the kinematic viscosity. We find typically $\mathcal{P}_{\text{diss}} \sim \mathcal{P}_{\text{inj}}/10$,
 124 meaning that most of the energy is dissipated by another mechanism than viscous dissipation
 125 of high-frequency waves in the bulk. We believe that this mechanism is linked with the
 126 nonlinear dynamics at large scales, which involves very steep structures acting as localized
 127 sources of dissipation (e.g., cusps of very steep slope).

128 3. Numerical model

129 To identify high-order nonlinear effects in the experimental data, these wave fields are
 130 reproduced numerically up to second-order nonlinearities. The elevation at a given location is
 131 computed as $\eta(t) = \eta^{(1)} + \eta^{(2)}$, where the linear contribution $\eta^{(1)}$ is the sum of $N_{\omega} \times N_{\theta} = 512$
 132 independent progressive waves ($N_{\omega} = 16$ angular frequencies, each of them associated with
 133 $N_{\theta} = 32$ directions), and $\eta^{(2)}$ is the nonlinear correction. More precisely, $\eta^{(1)}$ reads

$$134 \quad \eta^{(1)}(t) = \sum_{n_{\omega}=1}^{N_{\omega}} \sum_{n_{\theta}=1}^{N_{\theta}} a_{n_{\omega},n_{\theta}} \cos(-\omega_{n_{\omega}}t + \phi_{n_{\omega},n_{\theta}}), \quad (3.1)$$

135 where $a_{n_{\omega},n_{\theta}}$ are random numbers drawn from normal distributions of zero mean and
 136 standard deviations $A_{n_{\omega}}$. The phase constants $\phi_{n_{\omega},n_{\theta}}$ are uniformly distributed in the range

	Run 1			Run 2			Run 3		
	exp	num	th	exp	num	th	exp	num	th
σ (cm)	0.98	1.02		1.63	1.74		2.31	2.37	
\mathcal{S}	0.21	0.19	0.20	0.25	0.24	0.23	0.22	0.20	0.22
$K - 3$	0.18	0.06	0.06	0.20	0.09	0.07	0.17	0.07	0.04
ν	0.25	0.21		0.30	0.22		0.36	0.31	
f_0 (Hz)	1.68	1.60		1.43	1.37		1.18	1.13	
f_p (Hz)	1.38	1.35		1.15	1.20		0.90	0.90	
f_T (Hz)	1.59	1.54		1.33	1.31		1.06	1.04	
ε_T	0.10	0.10		0.12	0.12		0.11	0.10	
N_{tot}	3 779	963		3 385	889		2 548	368	
N_{RW}	937	840		899	798		475	450	

Table 1: Standard deviation σ , skewness \mathcal{S} , kurtosis K , dimensionless spectral bandwidth ν , mean frequency f_0 , peak frequency f_p , Tayfun frequency f_T and steepness ε_T based on f_T . “exp” denotes experimental measurements, “num” numerical models and “th” theoretical estimates given by Eq. (4.1) and (4.3) and computed based on the experimental PSD. The number of waves N_{tot} and rogue waves N_{RW} , defined as $H > 2H_S$ with $H_S = 4\sigma$, are also reported.

137 $[0, 2\pi]$. The leading-order nonlinear correction $\eta^{(2)}$ stems from Longuet-Higgins (1977) (up
 138 to a correction factor of one half, see Srokosz (1986)). In particular, it involves the wave
 139 vectors of the linear waves, set to model an isotropic wave field as

$$140 \quad \mathbf{k}_{n_\omega, n_\theta} = \frac{\omega_{n_\omega}^2}{g} \left[\cos\left(\frac{2\pi n_\theta}{N_\theta}\right) \mathbf{e}_x + \sin\left(\frac{2\pi n_\theta}{N_\theta}\right) \mathbf{e}_y \right]. \quad (3.2)$$

141 The angular frequencies $\{\omega_{n_\omega}\}$ are linearly distributed in a given range with $\Delta\omega =$
 142 $2\pi \times 0.1 \text{ rad} \cdot \text{s}^{-1}$. Both this range and the constants $\{A_{n_\omega}\}$ are adjusted to reproduce
 143 the experimental spectra at large scale, see Fig. 2. For each run, 5×10^7 values of $\eta(t = 0)$
 144 and millions of waves from time series of $\eta(t)$ with a time step of 0.01 s are computed from
 145 independent drawings of $\{a_{n_\omega, n_\theta}, \phi_{n_\omega, n_\theta}\}$. The former are used to obtain the data reported
 146 in Tab. 1 and Fig. 2-3 whereas waves are documented in Fig. 4 - 8.

147 4. Moments

148 The first moments of $\eta(t)$ from experiments and numerical models are reported in Tab. 1.
 149 The standard deviation $\sigma = \langle \eta^2 \rangle^{1/2}$ is found to increase with the forcing amplitude, while
 150 the skewness $\mathcal{S} = \langle \eta^3 \rangle / \sigma^3$ and the kurtosis $K = \langle \eta^4 \rangle / \sigma^4$ remain roughly constant. Other
 151 characteristics of sea states are computed, namely the dimensionless spectral bandwidth
 152 $\nu = (m_0 m_2 / m_1^2 - 1)^{1/2}$, with $m_n = \int S_\eta(f) f^n df$ the spectral moments, the mean frequency
 153 $f_0 = m_1 / m_0$, the peak frequency f_p , the Tayfun frequency $f_T = f_0 / [1 + \nu^2 (1 + \nu^2)^{-3/2}]$
 154 discussed later in the manuscript (Tayfun 1993; Tayfun & Fedele 2007) and the steepness
 155 $\varepsilon_T = (2\pi f_T)^2 \sigma / g$ based on f_T , with g the acceleration due to gravity. The dimensionless
 156 parameters measured experimentally (\mathcal{S} , K , ν and ε_T) correspond to typical values observed
 157 in the ocean, although field measurements yield $f_{0,p,T} = O(0.1)$ Hz and $\sigma = O(1)$ m
 158 (Christou & Ewans 2014). This confirms that the wave field under study shares the complex
 159 dynamics at work in the ocean while allowing the recording of ten times more waves over
 160 the same acquisition time.

161 The skewness \mathcal{S} can be compared with theoretical predictions. The linear model reduces
 162 surface elevation to a sum of independent progressive waves of various frequencies and

163 amplitudes ($\eta^{(1)}(t)$ in (3.1)), for which \mathcal{S} vanishes. In the 1960s, Longuet-Higgins computed
 164 the second-order nonlinear correction $\eta^{(2)}(t)$ and showed that it only involves non-resonant
 165 interactions, mathematically of the form of progressive waves that do not verify the linear
 166 dispersion relation, the so-called “bound waves” (Longuet-Higgins 1977). The skewness then
 167 becomes non-zero and can be inferred from $S_\eta(f)$: simplified under the assumption of an
 168 isotropic wave field, it reads

$$169 \quad \mathcal{S} = \int \frac{3k_1}{2\pi\sigma^3} S_\eta(k_1) S_\eta(k_2) I\left(\frac{k_2}{k_1}\right) dk_{1,2} \quad (4.1)$$

171 where I is an explicit function, see Appendix A. Further, assuming a narrowband frequency
 172 spectrum ($\nu \ll 1$, i.e., $f_0 = f_T = f_p$) numerically yields $\mathcal{S} = 2.07\varepsilon_T$, in contrast to $\mathcal{S} = 3\varepsilon_T$
 173 for unidirectional waves of a narrowband frequency spectrum. The theoretical prediction of
 174 \mathcal{S} computed from Eq. (4.1) together with the experimental PSD S_η is reported in Tab. 1: it
 175 accounts for both numerical models and experimental results.

176 Several decades later, Janssen built on the canonical transformation introduced in Zakharov
 177 (1968) to derive the surface elevation up to the next order and to consistently compute the
 178 deviation of the kurtosis from three (Janssen 2009). Disentangling resonant and non-resonant
 179 interactions, he obtained

$$180 \quad K = 3(1 + C_4^{\text{dyn}} + C_4^{\text{can}}), \quad (4.2)$$

181 where C_4^{dyn} results from four-wave resonant interactions and only allows analytic expressions
 182 for spectra that are narrow in frequency and direction (Fedele 2015; Janssen & Fedele 2019).
 183 In contrast, C_4^{can} is associated with bound waves and can be inferred directly from $S_\eta(f)$:
 184 for an isotropic wave field,

$$185 \quad C_4^{\text{can}} = \int \frac{k_1^2}{\pi^2\sigma^4} S_\eta(k_1) S_\eta(k_2) S_\eta(k_3) \psi\left(\frac{k_2}{k_1}, \frac{k_3}{k_1}\right) dk_{1,2,3}, \quad (4.3)$$

187 where ψ is another explicit function, see Appendix B. Furthermore, if the spectrum is
 188 narrowband in frequency, it reduces to $C_4^{\text{can}} = 2.75\varepsilon_T^2$. The theoretical values of $3C_4^{\text{can}}$
 189 computed from Eq. (4.3) and the experimental PSD S_η are reported in Tab. 1. They match
 190 our numerical models, in which no resonant interaction takes place, but strongly differs from
 191 experimental measurements. This demonstrates that four-wave interactions not only generate
 192 the low-frequency waves under study but also crucially affect their statistics. Note that a
 193 similar conclusion has been reached in a regime of capillary wave turbulence dominated by
 194 four-wave interactions (Xia *et al.* 2010; Shats *et al.* 2010).

195 5. Probability Density Functions (p.d.f.s)

196 The p.d.f.s of experimental and numerical normalized surface elevations $f(u = \eta/\sigma)$ are
 197 reported in Fig. 3, along with a normal law of zero mean and unit variance, a Tayfun law
 198 and two Gram-Charlier series. The normal distribution describes linear waves and accounts
 199 neither for the finite skewness nor for a kurtosis other than three. The Tayfun law corresponds
 200 to *unidirectional* and narrowband waves with second-order nonlinearities (Tayfun 1980), see
 201 Appendix C for its analytic expression. It only depends on the steepness ε_T and has been
 202 shown empirically to provide a fair estimate of the *tails* of $f(u)$ for isotropic and broadbanded
 203 waves as well, provided that ε_T is artificially tuned to generate the observed skewness (0.24
 204 in the case of Fig. 3 (left)) (Aubourg *et al.* 2017; Falcon *et al.* 2020). It is found here to fit
 205 the tails of the numerical p.d.f.s and to underestimate the experimental ones. This difference
 206 in the probability of extreme surface elevations translates into the difference in kurtosis

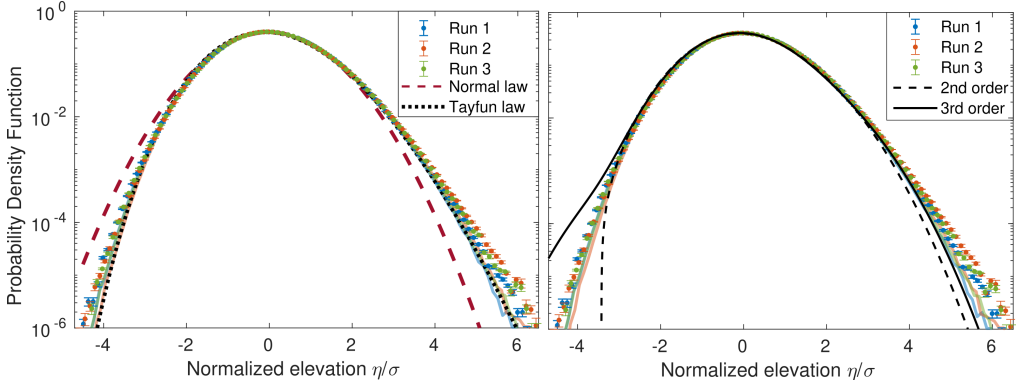


Figure 3: The p.d.f.s of the normalized surface elevation η/σ from experiments (symbols) and numerical models (thick coloured lines), compared with (left) a normal law and a Tayfun law and (right) the second- and third-order Gram-Charlier series computed with $S = K - 3 = 0.2$.

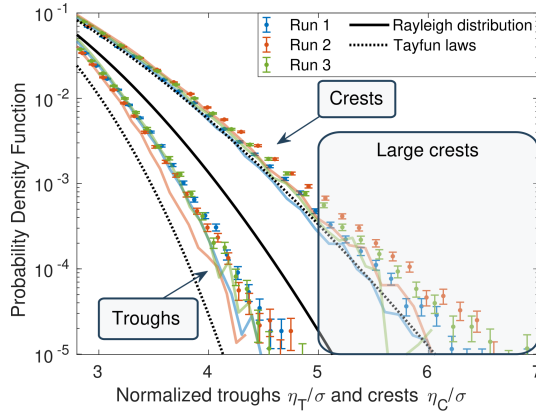


Figure 4: The p.d.f.s of the normalized wave troughs and crests compared with numerical models (thick coloured lines), a Rayleigh distribution (black solid line) and the first nonlinear corrections for unidirectional and narrowband waves (dotted lines).

207 discussed before. The p.d.f.s are also compared with the low-order Gram-Charlier series
 208 commonly used in theoretical work on surface waves, see Appendix D for definitions. They
 209 are reported in Fig. 3 (right) based on the typical experimental values $S = K - 3 = 0.2$
 210 from Tab. 1. As observed in Klahn *et al.* (2021), they both underestimate large positive values
 211 and fail to capture large negative ones (for which the p.d.f. is either undefined, as for the
 212 second-order Gram-Charlier approximation, or largely above the experimental data, as for
 213 the third-order approximation).

214 Time series are then analysed in terms of zero down-crossing waves, i.e. events separated
 215 by zero crossings ($\eta = 0$) in which η assumes negative then positive values (IAHR 1989).
 216 By definition, the wave height H is the sum of the wave trough η_T (taken positive) and wave
 217 crest η_C , the duration of the wave being the period T . In this manuscript, RWs are defined as
 218 waves for which $H > 2H_S$, with $H_S = 4\sigma$ the significant wave height, whereas large crests
 219 are defined by $\eta_C > 1.25H_S$. The threshold $1.25H_S = 5\sigma$ corresponds to an alternative
 220 definition of RWs in the literature (Fedele *et al.* 2016). The numbers of recorded waves and
 221 RWs are reported in Tab. 1.

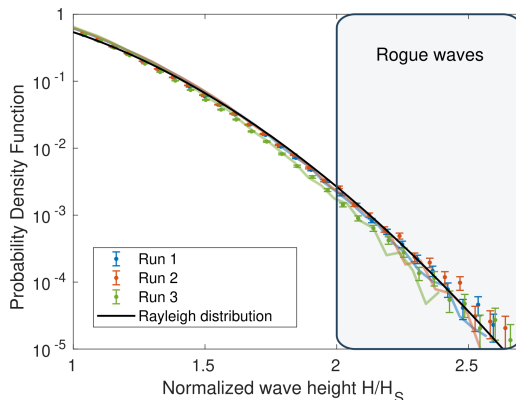


Figure 5: The p.d.f.s of the normalized wave height H/H_S from experiments (symbols) and numerical models (thick coloured lines), compared with a Rayleigh distribution.

222 Consider first the p.d.f. of η_C and η_T . For unidirectional and narrowband wave fields, they
 223 have been explicitly computed by Tayfun up to second-order nonlinearities (Tayfun 1980),
 224 see Appendix E for their analytic expressions. Similar to surface elevation, the p.d.f. of η_C
 225 has been empirically found to fit the tails of multidirectional wave fields as well (Soquet-
 226 Juglard *et al.* 2005; Denissenko *et al.* 2007; Klahn *et al.* 2021). Both experimental and
 227 numerical p.d.f.s are reported in Fig. 4 along with the theoretical Rayleigh distribution
 228 ($f_R(\xi) = \xi \exp(-\xi^2/2)$, capturing linear waves) and the Tayfun distributions with the
 229 steepness parameter tuned to describe a skewness of 0.24. Our numerical models with
 230 bound waves only indicate that the fortuitous agreement between Tayfun’s predictions for
 231 unidirectional waves and data from isotropic wave fields is restricted to crests. Moreover,
 232 one of the main outcomes of this work is that large crests are much more likely to be found
 233 experimentally than numerically or expected from the Tayfun law.

234 The wave height $H = \eta_C + \eta_T$ is then investigated. As routinely observed, the distribution
 235 of H/H_S as a function of the wave period T peaks close to the inverse Tayfun frequency
 236 f_T^{-1} (Tayfun 1993; Tayfun & Fedele 2007), see the additional figures in Appendix F. The
 237 experimental and numerical p.d.f.s of $u = H/H_S$, reported in Fig. 5, are compared with
 238 the Rayleigh distribution $f_R(u) = 4u \exp(-2u^2)$, which describes narrowband waves with
 239 no assumption on directionality and is valid even when the second-order nonlinearities are
 240 included (Longuet-Higgins 1952; Tayfun 1980). These data are all found to be similar. The
 241 wave height $H = \eta_C + \eta_T$ is therefore not only independent of second-order nonlinearities,
 242 as can be shown theoretically, but also seems to be largely independent of higher-order
 243 corrections. This is in sharp contrast with the statistics of η_C and η_T detailed above.

244 6. Shape of large crests

245 The mean surface elevation at a given position right before/after a large crest occurs (identified
 246 as $\eta(0)$ with time origin shifted such as the crest manifests at $t = 0$) is approximated at second
 247 order in the joint limit of small amplitude and frequency bandwidth as

$$248 \quad \eta(t) = \eta(0) \left[\frac{\Psi(t) + \frac{\eta_C \mathcal{F}(t)}{H_s}}{1 + \frac{\eta_C \mathcal{F}(0)}{H_s}} \right], \quad (6.1)$$

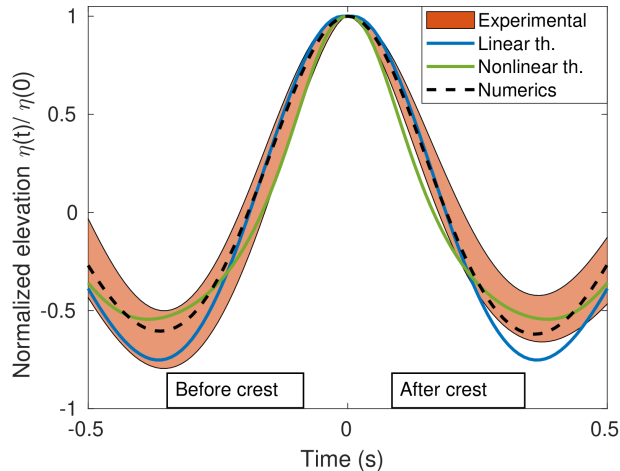


Figure 6: Shape of the large crests ($\eta(0) > 1.25H_S$) for Run 2. The coloured area corresponds to experiments (mean value \pm standard deviation), the black dashed line to numerical models and solid lines to first- and second-order theories. Similar figures for Run 1 and Run 3 are reported in Appendix F.

249 where $\Psi(t) = \langle \eta(0)\eta(t) \rangle / \sigma^2$ is the autocorrelation function, \mathcal{F} is a function of S_η detailed
 250 in Appendix G and η_C is the linear component of $\eta(0)$ (Fedele & Tayfun 2009). Previous
 251 studies have only tested this result in the linear limit in which $\eta_C = 0$ (Soquet-Juglard *et al.*
 252 2005; Klahn *et al.* 2021). The normalized elevation $\eta(t)/\eta(0)$ computed from Eq. (6.1) with
 253 both $\eta_C = 0$ and $\eta_C = 1.25H_S$ is reported in Fig. 6, along with experimental and numerical
 254 values for crests such that $\eta_C > 1.25H_S$. Our data confirm that the linear approximation
 255 overestimates the depths of the troughs preceding and following the crest, a discrepancy
 256 fixed with second-order corrections. However, both theoretical models are symmetric in
 257 time reversal (since $\Psi(t) = \Psi(-t)$ and $\mathcal{F}(t) = \mathcal{F}(-t)$) whereas experimental measurements
 258 before and after the crest occurs persistently differ. This asymmetry also manifests in steeper
 259 slopes before the crests ($t < 0$) than after ($t > 0$). The numerical simulations of Fujimoto
 260 *et al.* (2019) have shown that, at a fixed time and for directional wave fields, high crests are
 261 not symmetric in space as a result of the four-wave resonant interactions not captured by the
 262 second-order model reported in Eq. (6.1).

263 7. Conclusion

264 Laboratory experiments with simplified directional spectra provide useful hints about
 265 the various processes taking place in the ocean without the usual bias of, e.g., wave
 266 breaking regularization in numerical simulations or varying environmental conditions in field
 267 measurements. In this study, more than two thousands RWs were observed in statistically
 268 homogeneous, isotropic and steady wave fields, allowing the predictions of commonly used
 269 theoretical models to be confronted with data in which strongly nonlinear events take place.
 270 To highlight the consequences of these high-order nonlinearities, numerical simulations
 271 associated with similar PSDs and valid up to second order were carried out. Therefore, they
 272 include the leading-order bound wave correction but not the resonant interactions.

273 The third and fourth normalized moments of surface elevation are compared with
 274 theoretical results in which the leading-order bound wave correction is accounted for. These
 275 analytic expressions are found to accurately describe the skewness of both experimental and
 276 numerical data. However, they significantly underestimate the experimental kurtosis while

277 being in agreement with the numerical ones, evidencing a first consequence of resonant
 278 interactions on the statistics. This discrepancy is also manifest in the tails of the normalized
 279 surface elevation p.d.f.s.

280 The surface elevation time series are then split into individual waves whose heights, crests
 281 and troughs are analysed. The wave height is found to be robust to high-order effects, the
 282 experimental p.d.f.s being similar to the numerical ones and to the Rayleigh distribution.
 283 A similar conclusion cannot be drawn regarding the wave crests and troughs, for which
 284 large values are much more likely experimentally than numerically, indicating that four-wave
 285 resonant interactions strongly affect their statistics. The impact of high-order nonlinearities
 286 on large crests is further evidenced through the comparison of their mean shape with first-
 287 and second-order theoretical predictions, none of them being able to capture the asymmetry
 288 under time reversal. Therefore, the phenomenology of rogue waves crucially depend on how
 289 they are defined: high-order nonlinear effects do not seem to play a significant role if the
 290 wave height criterion $H > 8\sigma$ is used, whereas for RW depicted as $\eta_C > 5\sigma$ (referred to as
 291 ‘large crests’ in this paper) they significantly enhance their probability of occurrence. This
 292 finding demonstrates the current need for higher-order theoretical models that disentangle
 293 troughs and crests.

294 Note that, as reported in previous studies (Aubourg *et al.* 2017; Falcon *et al.* 2020; Soquet-
 295 Juglard *et al.* 2005; Denissenko *et al.* 2007; Klahn *et al.* 2021), some features of our second-
 296 order numerical model of *isotropic* waves are surprisingly well fitted by theoretical models
 297 derived for *unidirectional* and narrowband wave fields, provided that the single parameter
 298 they depend on, the steepness ε_T , is tuned to generate the observed skewness. This applies
 299 to the tails of the PDFs of both the normalized surface elevation and wave crests, but not to
 300 the wave troughs.

301 Many geophysical processes that are both challenging to model theoretically and to
 302 disentangle from other effects in field experiments could benefit from similar investigations
 303 with these isotropic nonlinear steady states. This includes, but is not limited to, the impact
 304 of waves on mixing and air-sea fluxes, the effect of rain in calming the sea and the effective
 305 parameters of random nonlinear waves (diffusion of a pollutant, damping and scattering of a
 306 wave train, etc.).

307 We thank the technical team at the ECN facilities for their help and support on the
 308 experimental setup. Part of this work was supported by the French National Research
 309 Agency (ANR DYSTURB Project No. ANR-17-CE30-0004), and by a grant from the Simons
 310 Foundation MPS No. 651463-Wave Turbulence.

311 Declaration of Interests: The authors report no conflict of interest.

312 Appendix A. Detail on equation (4.1)

313 Following Janssen (2009) and its notations, the third moment of the surface elevation μ_3 is
 314 related to the standard deviation $\sqrt{\mu_2}$ and to the skewness parameter C_3 through its Eqs. (51)
 315 and (52), that are

$$316 \quad C_3 = \frac{\mu_3}{\mu_2^{3/2}} = \frac{3}{m_0^{3/2}} \int d\mathbf{k}_{1,2} E_1 E_2 (\mathcal{A}_{1,2} + \mathcal{B}_{1,2}), \quad (\text{A } 1)$$

317 where $m_0 = \int d\mathbf{k}_1 E_1$ and $E(\mathbf{k})$ is the first-order spectrum. After lengthy but straightforward
 318 computations using various equations of Janssen (2009), we obtain the transfer coefficients

319 $\mathcal{A}_{1,2}(\mathbf{k}_1, \mathbf{k}_2)$ and $\mathcal{B}_{1,2}(\mathbf{k}_1, \mathbf{k}_2)$ for deep-water gravity waves

$$320 \quad \mathcal{A}_{1,2} = \frac{1}{\sqrt{k_1 k_2}} \left[\frac{\left(\sqrt{k_1} + \sqrt{k_2} \right)^2 (\mathbf{k}_1 \cdot \mathbf{k}_2 - k_1 k_2)}{(\sqrt{k_1} + \sqrt{k_2})^2 - |\mathbf{k}_1 + \mathbf{k}_2|} - \left(\frac{\mathbf{k}_1 \cdot \mathbf{k}_2 - k_1 k_2 - \sqrt{k_1 k_2} (k_1 + k_2)}{2} \right) \right], \quad (\text{A } 2)$$

$$321 \quad \mathcal{B}_{1,2} = \frac{1}{\sqrt{k_1 k_2}} \left[\frac{(\sqrt{k_1} - \sqrt{k_2})^2 (\mathbf{k}_1 \cdot \mathbf{k}_2 + k_1 k_2)}{(\sqrt{k_1} - \sqrt{k_2})^2 - |\mathbf{k}_1 - \mathbf{k}_2|} - \left(\frac{\mathbf{k}_1 \cdot \mathbf{k}_2 + k_1 k_2 - \sqrt{k_1 k_2} (k_1 + k_2)}{2} \right) \right]. \quad (\text{A } 3)$$

322

323 It can be readily confirmed that this expression of the skewness corresponds to the one initially
 324 derived by Longuet-Higgins (Eq. (3.11) of Longuet-Higgins (1977) corrected by a misprint
 325 of one half). Given that the wave field is assumed isotropic, $E(\mathbf{k})d\mathbf{k} = S_\eta(k)/(2\pi)dkd\theta$,
 326 with $S_\eta(k)$ the surface elevation PSD. Moreover, since the transfer coefficients are invariant
 327 by a simultaneous rotation of \mathbf{k}_1 and \mathbf{k}_2 , eq. (A 1) reduces to

$$328 \quad C_3 = \frac{3}{m_0^{3/2}} \int_0^{2\pi} d\theta \iint dk_1 dk_2 \frac{S_\eta(k_1)S_\eta(k_2)}{2\pi\sqrt{k_1 k_2}} \quad (\text{A } 4)$$

$$329 \quad \left[\frac{\left(\sqrt{k_1} + \sqrt{k_2} \right)^2 (\mathbf{k}_1 \cdot \mathbf{k}_2 - k_1 k_2)}{(\sqrt{k_1} + \sqrt{k_2})^2 - |\mathbf{k}_1 + \mathbf{k}_2|} + \frac{(\sqrt{k_1} - \sqrt{k_2})^2 (\mathbf{k}_1 \cdot \mathbf{k}_2 + k_1 k_2)}{(\sqrt{k_1} - \sqrt{k_2})^2 - |\mathbf{k}_1 - \mathbf{k}_2|} - \mathbf{k}_1 \cdot \mathbf{k}_2 + \sqrt{k_1 k_2} (k_1 + k_2) \right], \quad 330$$

331 with $\mathbf{k}_1 = k_1 \mathbf{e}_x$ and $\mathbf{k}_2 = k_2 (\cos \theta \mathbf{e}_x + \sin \theta \mathbf{e}_y)$. Define a function I such that

$$332 \quad I(\alpha) = \int_0^{2\pi} d\theta \left[\frac{\sqrt{\alpha} (1 + \sqrt{\alpha})^2 (\cos \theta - 1)}{(1 + \sqrt{\alpha})^2 - \sqrt{1 + \alpha^2} + 2\alpha \cos \theta} + \frac{\sqrt{\alpha} (1 - \sqrt{\alpha})^2 (\cos \theta + 1)}{(1 - \sqrt{\alpha})^2 - \sqrt{1 + \alpha^2} - 2\alpha \cos \theta} + (1 + \alpha) \right], \quad (\text{A } 5)$$

333 and (A 4) then reads

$$334 \quad C_3 = \frac{3}{m_0^{3/2}} \iint \frac{S_\eta(k_1)S_\eta(k_2)k_1}{2\pi} I\left(\frac{k_2}{k_1}\right) dk_1 dk_2, \quad (\text{A } 6)$$

335 which corresponds, with $C_3 \rightarrow \mathcal{S}$ and $m_0 \rightarrow \sigma^2$ (our notations), to Eq. (4.1).

336 Appendix B. Detail on equation (4.3)

337 A similar procedure can be applied to compute the canonical contribution to the kurtosis
 338 from Eq. (59) of Janssen (2009) ,

$$339 \quad C_4^{\text{can}} = \frac{4}{m_0^2} \int E(\mathbf{k}_1)E(\mathbf{k}_2)E(\mathbf{k}_3)\Psi(\mathbf{k}_1, \mathbf{k}_2, \mathbf{k}_3)d\mathbf{k}_1 d\mathbf{k}_2 d\mathbf{k}_3, \quad (\text{B } 1)$$

340 where Ψ is an explicit interaction coefficient not detailed here. With $E(\mathbf{k}_i) =$
 341 $S_\eta(k_i)/(2\pi)dk_i d\theta_i$ and $\sigma^2 = m_0$,

$$342 \quad C_4^{\text{can}} = \frac{4}{(2\pi)^3 \sigma^4} \int S_\eta(k_1)S_\eta(k_2)S_\eta(k_3)\Psi(\mathbf{k}_1, \mathbf{k}_2, \mathbf{k}_3)dk_1 dk_2 dk_3 d\theta_1 d\theta_2 d\theta_3. \quad (\text{B } 2)$$

343 Since Ψ is invariant under a simultaneous rotation of \mathbf{k}_1 , \mathbf{k}_2 and \mathbf{k}_3 , a first integration can be
344 performed

$$345 \quad C_4^{\text{can}} = \frac{4}{(2\pi)^2\sigma^4} \int S_\eta(k_1)S_\eta(k_2)S_\eta(k_3)\Psi(k_1\mathbf{e}_x, \mathbf{k}_2, \mathbf{k}_3)dk_1dk_2dk_3d\theta_2d\theta_3, \quad (\text{B } 3)$$

346 with $\mathbf{k}_{2,3} = k_{2,3} (\cos \theta_{2,3}\mathbf{e}_x + \sin \theta_{2,3}\mathbf{e}_y)$. Finally, note that the function Ψ is such that

$$347 \quad \Psi(k_1\mathbf{e}_x, \mathbf{k}_2, \mathbf{k}_3) = k_1^2\Psi\left(\mathbf{e}_x, \frac{\mathbf{k}_2}{k_1}, \frac{\mathbf{k}_3}{k_1}\right), \quad (\text{B } 4)$$

348 and define a function ψ by

$$349 \quad \psi(\alpha, \beta) = \int \Psi(\mathbf{e}_x, \alpha [\cos \theta_2\mathbf{e}_x + \sin \theta_2\mathbf{e}_y], \beta [\cos \theta_3\mathbf{e}_x + \sin \theta_3\mathbf{e}_y]) d\theta_2d\theta_3. \quad (\text{B } 5)$$

350 The coefficient C_4^{can} then reads

$$351 \quad C_4^{\text{can}} = \frac{4}{(2\pi)^2\sigma^4} \int S_\eta(k_1)S_\eta(k_2)S_\eta(k_3)k_1^2\psi\left(\frac{k_2}{k_1}, \frac{k_3}{k_1}\right)dk_1dk_2dk_3, \quad (\text{B } 6)$$

352 which corresponds to Eq. (4.3).

353 Appendix C. Tayfun p.d.f. of surface elevation

354 The p.d.f. of surface elevation can be explicitly computed in the case of a unidirectional and
355 narrowband wave field in which only the first nonlinear correction is computed. However,
356 several misprints make the expression of this PDF difficult to obtain from the literature. In
357 particular, the original derivation of Tayfun (1980) must be corrected as follows: his Eq. (24)
358 should read

$$359 \quad F_\xi(u) = (2\pi)^{-1/2} \int_{\alpha(u)}^{\infty} e^{-\tau^2/2} \{\text{erf}[A(\tau, u) + \beta] + \text{erf}[A(\tau, u) - \beta]\} d\tau, \quad (\text{C } 1)$$

360 and his corrected Eq. (27) is

$$361 \quad A(\tau, u) = \beta\sqrt{1 + \frac{\sqrt{2}\gamma u}{\beta} + \frac{\tau^2}{2\beta^2}}. \quad (\text{C } 2)$$

362 Note also that only approximate expressions of this p.d.f. are reported in Soquet-Juglard
363 *et al.* (2005) : indeed, their Eq. (7) becomes undefined for large negative values of the surface
364 elevation (if their $1 + 2\sigma z < 0$, their $C(0)$ required in the integral is no longer real valued).

365 For completeness, the full set of equations required to compute the p.d.f. $f(u)$ of the
366 normalized surface elevation $u = \eta/\sigma$ ($\sigma = \langle \eta^2 \rangle^{1/2}$) is reported below

$$367 \quad f(u) = \frac{dF}{du}, \quad F(u) = \frac{1}{\sqrt{2\pi}} \int_{\alpha(u)}^{\infty} e^{-\frac{\tau^2}{2}} [\text{erf}(A(\tau, u) + \beta) + \text{erf}(A(\tau, u) - \beta)] d\tau \quad (\text{C } 3)$$

368 with

$$369 \quad A(\tau, u) = \beta\sqrt{1 + \frac{\sqrt{2}\gamma u}{\beta} + \frac{\tau^2}{2\beta^2}}, \quad \beta = \frac{1}{\sqrt{-1 + \sqrt{1 + 4\sigma^2 k^2}}}, \quad \gamma = \sqrt{\frac{1 + \sqrt{1 + 4\sigma^2 k^2}}{2}}, \quad (\text{C } 4)$$

370 and

$$371 \quad \alpha\left(u \geq -\frac{\beta}{\sqrt{2}\gamma}\right) = 0, \quad \alpha\left(u < -\frac{\beta}{\sqrt{2}\gamma}\right) = \beta\sqrt{-2\left(1 + \frac{\sqrt{2}\gamma u}{\beta}\right)}. \quad (\text{C } 5)$$

372 **Appendix D. Second- and third-order Gram-Charlier series**

373 A theoretical approach to the p.d.f. of surface elevation consists in using low-order Gram-
 374 Charlier series. Following Klahn *et al.* (2021), we define in this manuscript the second-order
 375 approximation as

$$376 \quad f_{GC2} \left(u = \frac{\eta}{\sigma} \right) = \frac{1}{\sqrt{2\pi}} e^{-u^2/2} \left[1 + \frac{\mathcal{S}}{6} H_3(u) \right], \quad H_3(u) = u^3 - 3u, \quad (\text{D } 1)$$

377 and the third-order one

$$378 \quad f_{GC3} \left(u = \frac{\eta}{\sigma} \right) = \frac{1}{\sqrt{2\pi}} e^{-u^2/2} \left[1 + \frac{\mathcal{S}}{6} H_3(u) + \frac{1}{24} (K - 3) H_4(u) + \frac{1}{72} \mathcal{S}^2 H_6(u) \right], \quad (\text{D } 2)$$

379 with

$$380 \quad H_4(u) = u^4 - 6u^2 + 3, \quad H_6(u) = u^6 - 15u^4 + 45u^2 - 15. \quad (\text{D } 3)$$

381 **Appendix E. Tayfun p.d.f. of the crests and troughs**

382 For unidirectional and narrowband wave fields, the p.d.f. of crests accounting for second-
 383 order nonlinearities reads (Tayfun 1980)

$$384 \quad f_C(\xi_C) = \frac{2\varepsilon}{-1 + \sqrt{1 + 4\varepsilon^2}} \left(1 - \frac{1}{\sqrt{1 + 2\varepsilon\xi_C}} \right) \exp \left[-\frac{\left(-1 + \sqrt{1 + 2\varepsilon\xi_C} \right)^2}{-1 + \sqrt{1 + 4\varepsilon^2}} \right], \quad (\text{E } 1)$$

385 with $\xi_C = \eta_C/\sigma$ and $\sigma = \langle \eta^2 \rangle^{1/2}$ (note that the PDF reported in Tayfun (1980) considers
 386 instead the wave crest normalized by the standard deviation of the linear component). The
 387 steepness parameter $\varepsilon = \sigma k$, with k the central wavenumber of the narrowband wave fields,
 388 is in that case related to the skewness $\mathcal{S} = 3\varepsilon + O(\varepsilon^3)$. Similarly, for the troughs,

$$389 \quad f_T(\xi_T) = \frac{-2\varepsilon}{-1 + \sqrt{1 + 4\varepsilon^2}} \left(1 - \frac{1}{\sqrt{1 - 2\varepsilon\xi_T}} \right) \exp \left[-\frac{\left(-1 + \sqrt{1 + 2\varepsilon\xi_T} \right)^2}{-1 + \sqrt{1 + 4\varepsilon^2}} \right], \quad (\text{E } 2)$$

390 with $\xi_T = \eta_T/\sigma$.

391 **Appendix F. Additional wave features**

392 The raw data of the normalized wave height H/H_S plotted versus the wave period T are
 393 reported in Fig. 7, while the shape of the large crests for Runs 1, 2 and 3 are shown in Fig. 8

394 **Appendix G. Expected shape of large waves**

395 From Eq. (5.7) of Fedele & Tayfun (2009), define in the deep-water and isotropic limit the
 396 function

$$397 \quad \mathcal{F}(t) = \frac{2}{(2\pi)^2 \sigma^3} \int S_\eta(k_1) S_\eta(k_2) \\
 398 \quad \left[(\mathcal{A}_{1,2} + \mathcal{B}_{1,2}) \cos(\omega_1 t) \cos(\omega_2 t) - (\mathcal{A}_{1,2} - \mathcal{B}_{1,2}) \sin(\omega_1 t) \sin(\omega_2 t) \right] dk_1 dk_2 d\theta_1 d\theta_2, \\
 399 \quad (\text{G } 1)$$

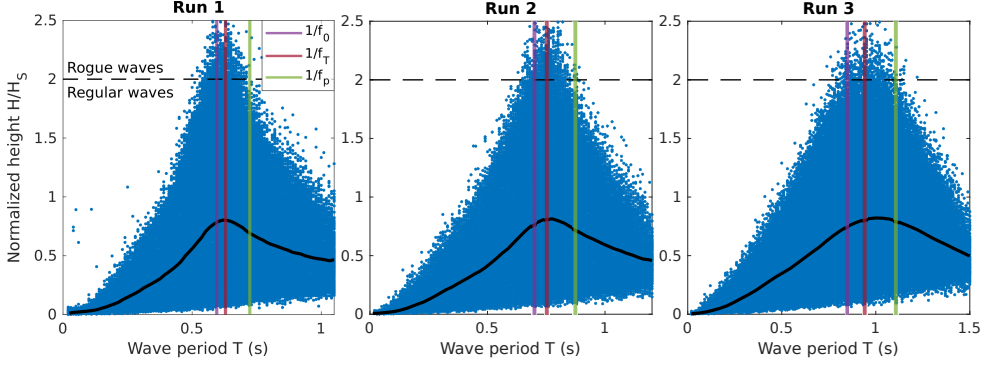


Figure 7: Experimental normalized wave height as a function of the wave period. The mean value is plotted in thick black and peaks close to the Tayfun period $1/f_T$. Vertical lines indicate f_0^{-1} , f_T^{-1} and f_p^{-1} ($f_0^{-1} < f_T^{-1} < f_p^{-1}$)

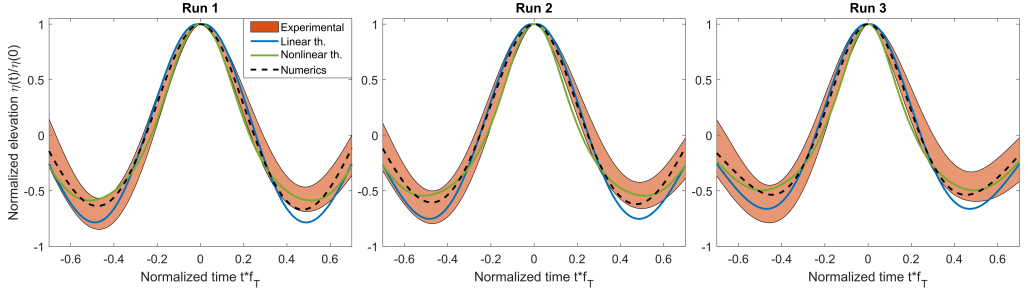


Figure 8: Shape of large crests ($\eta(0) > 1.25H_S$) for Runs 1, 2 and 3. The coloured area corresponds to experiments (mean value \pm standard deviation), the black dashed line to numerical models and solid lines to first- and second-order theories. The central figure corresponds to Fig. 6.

400 with $\omega_{1,2} = \sqrt{gk_{1,2}}$. A first angular integration can be performed to obtain

$$401 \quad \mathcal{F}(t) = \frac{1}{\pi\sigma^3} \int S_\eta(k_1)S_\eta(k_2)$$

$$402 \quad \left[(\mathcal{A}_{1,2} + \mathcal{B}_{1,2}) \cos(\omega_1 t) \cos(\omega_2 t) - (\mathcal{A}_{1,2} - \mathcal{B}_{1,2}) \sin(\omega_1 t) \sin(\omega_2 t) \right] dk_1 dk_2 d\theta, \quad (G 2)$$

403
404 with $\mathbf{k}_1 = k_1 \mathbf{e}_x$ and $\mathbf{k}_2 = k_2 (\cos \theta \mathbf{e}_x + \sin \theta \mathbf{e}_y)$. Further assume

$$405 \quad J(\alpha) = \sqrt{\alpha} \int_0^{2\pi} d\theta \left[\frac{(1 + \sqrt{\alpha})^2 (\cos \theta - 1)}{(1 + \sqrt{\alpha})^2 - \sqrt{1 + \alpha^2 + 2\alpha \cos \theta}} - \frac{(1 - \sqrt{\alpha})^2 (\cos \theta + 1)}{(1 - \sqrt{\alpha})^2 - \sqrt{1 + \alpha^2 - 2\alpha \cos \theta}} + 2 \right], \quad (G 3)$$

406 to obtain

$$407 \quad \mathcal{F}(t) = \frac{1}{\pi\sigma^3} \int S_\eta(k_1)S_\eta(k_2) k_1 \left[I\left(\frac{k_2}{k_1}\right) \cos(\omega_1 t) \cos(\omega_2 t) - J\left(\frac{k_2}{k_1}\right) \sin(\omega_1 t) \sin(\omega_2 t) \right] dk_1 dk_2 \quad (G 4)$$

408 which allows simple numerical integration. The elevation profile $\eta(t)$ close to a crest of linear
409 elevation ξ_c then follows from Eq. (5.10) of Fedele & Tayfun (2009) and reads at leading

410 order

$$411 \quad \eta(t) = \xi_c \Psi(t) + \frac{\xi_c^2 \mathcal{F}(t)}{4\sigma}, \quad (\text{G } 5)$$

412 with $\Psi(t) = \langle \eta(0)\eta(t) \rangle / \sigma^2$ the autocorrelation function.

413

REFERENCES

- 414 ABLOWITZ, M. J. & COLE, J. T. 2021 Transverse instability of rogue waves. *Phys. Rev. Lett.* **127**, 104101.
- 415 ADCOCK, T. A. A. & TAYLOR, P. H. 2014 The physics of anomalous (‘rogue’) ocean waves. *Rep. Prog. Phys.*
416 **77**, 105901.
- 417 AUBOURG, Q., CAMPAGNE, A., PEUREUX, C., ARDHUIN, F., SOMMERIA, J., VIBOUD, S. & MORDANT, N. 2017
418 Three-wave and four-wave interactions in gravity wave turbulence. *Phys. Rev. Fluids* **2**, 114802.
- 419 BADULIN, S. I. & IVONIN, D. V. 2012 Three-dimensional freak waves. Once more on new year wave. *Fund.*
420 *Prikl. Gidrofiz.* **5**, 37–51.
- 421 BENJAMIN, T. B. & FEIR, J. E. 1967 The disintegration of wave trains on deep water part 1. theory. *J. Fluid*
422 *Mech.* **27**, 417–430.
- 423 CAMPAGNE, A., HASSAINI, R., REDOR, I., SOMMERIA, J., VALRAN, T., VIBOUD, S. & MORDANT, N. 2018
424 Impact of dissipation on the energy spectrum of experimental turbulence of gravity surface waves.
425 *Phys. Rev. Fluids* **3**, 044801.
- 426 CAZAUBIEL, A., MICHEL, G., LEPOT, S., SEMIN, B., AUMAÎTRE, S., BERHANU, M., BONNEFOY, F. & FALCON,
427 E. 2018 Coexistence of solitons and extreme events in deep water surface waves. *Phys. Rev. Fluids*
428 **3**, 114802.
- 429 CHABCHOUB, A., GENTY, G., DUDLEY, J. M., KIBLER, B., & WASEDA, T. 2017 Experiments on spontaneous
430 modulation instability in hydrodynamics. In *Proceedings of The Twenty-Seventh International Ocean*
431 *and Polar Engineering Conference*, p. 420–424. San Francisco, ISOPE, Cupertino, 2017.
- 432 CHRISTOU, M. & EWANS, K. 2014 Field measurements of rogue water waves. *J. Phys. Oceanogr.* **44**,
433 2317–2335.
- 434 DEIKE, L., MIQUEL, B., GUTIÉRREZ, P., JAMIN, T., SEMIN, B., BERHANU, M., FALCON, E. & BONNEFOY, F.
435 2015 Role of the basin boundary conditions in gravity wave turbulence. *J. Fluid Mech.* **781**, 196–225.
- 436 DEMATTEIS, G., GRAFKE, T., ONORATO, M. & VANDEN-EIJNDEN, E. 2019 Experimental evidence of
437 hydrodynamic instantons: The universal route to rogue waves. *Phys. Rev. X* **9**, 041057.
- 438 DENISSENKO, P., LUKASCHUK, S. & NAZARENKO, S. 2007 Gravity wave turbulence in a laboratory flume.
439 *Phys. Rev. Lett.* **99**, 014501.
- 440 DUCROZET, G., ABDOLAHPOUR, M., NELLI, F. & TOFFOLI, A. 2021 Predicting the occurrence of rogue waves
441 in the presence of opposing currents with a high-order spectral method. *Phys. Rev. Fluids* **6**, 064803.
- 442 FALCON, E., MICHEL, G., PRABHUDESAI, G., CAZAUBIEL, A., BERHANU, M., MORDANT, N., AUMAÎTRE, S. &
443 BONNEFOY, F. 2020 Saturation of the inverse cascade in surface gravity-wave turbulence. *Phys. Rev.*
444 *Lett.* **125**, 134501.
- 445 FALCON, E. & MORDANT, N. 2022 Experiments in surface gravity-capillary wave turbulence. *Ann. Rev. Fluid*
446 *Mech.* **54**, 1–25.
- 447 FEDELE, F. 2015 On the kurtosis of deep-water gravity waves. *J. Fluid Mech.* **782**, 25–36.
- 448 FEDELE, F., BRENNAN, J., DE LEÓN, S. P., DUDLEY, J. & DIAS, F. 2016 Real world ocean rogue waves
449 explained without the modulation instability. *Sci. Reports* **6**, 27715.
- 450 FEDELE, F. & TAYFUN, A. 2009 On nonlinear wave groups and crest statistics. *J. Fluid Mech.* **620**, 221–239.
- 451 FORRISTALL, G. Z. 1978 On the statistical distribution of wave heights in a storm. *J. Geophys. Res.* **83**,
452 2353–2358.
- 453 FUJIMOTO, W., WASEDA, T. & WEBB, A. 2019 Impact of the four-wave quasi-resonance on freak wave shapes
454 in the ocean. *Ocean Dynamics* **69**, 101–121.
- 455 GRAMSTAD, O. & TRULSEN, K. 2007 Influence of crest and group length on the occurrence of freak waves.
456 *J. Fluid Mech.* **582**, 463–472.
- 457 IAHR, WORKING GROUP 1989 List of sea-state parameters. *J. Wtrway, Port, Coast., and Oc. Engrg.* **115** (6),
458 793–808.
- 459 JANSSEN, P. & FEDELE, F. 2019 Asymptotics for the long-time evolution of kurtosis of narrow-band ocean
460 waves. *J. Fluid Mech.* **859**, 790–818.

- 461 JANSSEN, P. A. E. M. 2009 On some consequences of the canonical transformation in the hamiltonian theory
462 of water waves. *J. Fluid Mech.* **637**, 1–44.
- 463 KARPADAKIS, I., SWAN, C. & CHRISTOU, M. 2020 Assessment of wave height distributions using an
464 extensive field database. *Coast. Eng.* **157**, 103630.
- 465 KLAHN, M., MADSEN, P. A. & FUHRMAN, D. R. 2021 On the statistical properties of surface elevation,
466 velocities and accelerations in multi-directional irregular water waves. *J. Fluid Mech.* **910**, A23.
- 467 LAKE, B. M., YUEN, H. C., RUNGALDIER, H. & FERGUSON, W. E. 1977 Nonlinear deep-water waves: theory
468 and experiment. part 2. evolution of a continuous wave train. *J. Fluid Mech.* **83**, 49–74.
- 469 LIGHTHILL, M. J. 1965 Contributions to the theory of waves in non-linear dispersive systems. *J. Inst. Maths
470 Applics* **1**, 269–306.
- 471 LONGUET-HIGGINS, M. S. 1952 On the statistical distribution of sea waves. *J. Mar. Res.* **11**, 245–266.
- 472 LONGUET-HIGGINS, M. S. 1977 The effect of non-linearities on statistical distributions in the theory of sea
473 waves. *J. Fluid Mech.* **17**, 459–480.
- 474 LUKASCHUK, S., NAZARENKO, S., McLELLAND, S. & DENISSENKO, P. 2009 Gravity wave turbulence in wave
475 tanks: Space and time statistics. *Phys. Rev. Lett.* **103**, 044501.
- 476 MELVILLE, W. K. 1982 The instability and breaking of deep-water waves. *J. Fluid Mech.* **115**, 165–185.
- 477 MICHEL, G., BONNEFOY, F., DUCROZET, G., PRABHUDESAI, G., CAZAUBIEL, A., COPIE, F., TIKAN, A., SURET,
478 P., RANDOUX, S. & FALCON, E. 2020 Emergence of peregrine solitons in integrable turbulence of
479 deep water gravity waves. *Phys. Rev. Fluids* **5**, 082801.
- 480 MILES, J. W. 1967 Surface-wave damping in closed basins. *Proc. Roy. Soc. A* **297**, 459–475.
- 481 NAZARENKO, S., LUKASCHUK, S., McLELLAND, S. & DENISSENKO, P. 2010 Statistics of surface gravity wave
482 turbulence in the space and time domains. *J. Fluid Mech.* **642**, 395–420.
- 483 ONORATO, M., CAVALERI, L., FOUQUES, S., GRAMSTAD, O., JANSSEN, P. A. E. M., MONBALIU, J., OSBORNE,
484 A. R., PAKOZDI, C., SERIO, M., STANSBERG, C. T., TOFFOLI, A. & TRULSEN, K. 2009 Statistical
485 properties of mechanically generated surface gravity waves: a laboratory experiment in a three-
486 dimensional wave basin. *J. Fluid Mech.* **627**, 235–257.
- 487 ONORATO, M., OSBORNE, A., SERIO, M. & CAVALERI, L. 2005 Modulational instability and non-gaussian
488 statistics in experimental random water-wave train. *Phys. Fluids* **17**, 078101.
- 489 ONORATO, M., OSBORNE, A., SERIO, M., CAVALERI, L., BRANDINI, C. & STANSBERG, C. T. 2004 Observation
490 of strongly non-gaussian statistics for random sea surface gravity waves in wave flume experiments.
491 *Phys. Rev. E* **70**, 067302.
- 492 ONORATO, M., OSBORNE, A. R. & SERIO, M. 2002 Extreme wave events in directional, randomoceanic sea
493 states. *Phys. Fluids* **14**, L25.
- 494 ONORATO, M., OSBORNE, A. R., SERIO, M., CAVALERI, L., BRANDINI, C. & STANSBERG, C. T. 2006 Extreme
495 waves, modulational instability and second order theory: wave flume experiments on irregular waves.
496 *Euro. J. Mech. B Fluids* **25**, 586–601.
- 497 SHATS, M., PUNZMANN, H. & XIA, H. 2010 Capillary rogue waves. *Phys. Rev. Lett.* **104**, 104503.
- 498 SHEMER, L. & SERGEEVA, A. 2009 An experimental study of spatial evolution of statistical parameters in a
499 unidirectional narrow-banded random wavefield. *J. Geophys. Res.* **114**, C01015.
- 500 SHEMER, L., SERGEEVA, A. & LIBERZON, D. 2010a Effect of the initial spectrum on the spatial evolution of
501 statistics of unidirectional nonlinear random waves. *J. Geophys. Res.* **115**, C12039.
- 502 SHEMER, L., SERGEEVA, A. & SLUNYAEV, A. 2010b Applicability of envelope model equations for simulation
503 of narrow-spectrum unidirectional random wave field evolution: Experimental validation. *Phys.
504 Fluids* **22**, 016601.
- 505 SOQUET-JUGLARD, H., DYSTHE, K., TRULSEN, K., KROGSTAD, H. E. & LIU, J. 2005 Probability distributions
506 of surface gravity waves during spectral changes. *J. Fluid Mech.* **542**, 192–195.
- 507 SROKOSZ, M. A. 1986 On the joint distribution of surface elevation and slopes for a nonlinear random sea,
508 with an application to radar altimetry. *J. Geophys. Res.* **91**, 995–1006.
- 509 TAYFUN, M. A. 1980 Narrow-band nonlinear sea waves. *J. Geophys. Res.* **85**, 1548–1552.
- 510 TAYFUN, M. A. 1993 Joint distribution of large wave heights and associated periods. *J. Wtrway, Port, Coast,
511 and Oc. Engrg.* **119**, 261–273.
- 512 TAYFUN, M. A. & FEDELE, F. 2007 Wave-height distributions and nonlinear effects. *Ocean Eng.* **34**, 1631–
513 1649.
- 514 TOFFOLI, A., BITNER-GREGERSEN, E., ONORATO, M. & BABANIN, A. V. 2008 Wave crest and trough
515 distributions in a broad-banded directional wave field. *Ocean Eng.* **35**, 1784–1792.
- 516 TOFFOLI, A., WASEDA, T., HOUTANI, H., CALAVERI, L., GREAVES, D. & ONORATO, M. 2015 Rogue waves in

- 517 opposing currents: an experimental study on deterministic and stochastic wave train. *J. Fluid Mech.*
518 **769**, 277–297.
- 519 WASEDA, T. 2006 Impact of directionality on the extreme wave occurrence in a discrete random wave system.
520 *9th Intl Workshop on Wave Hindcasting and Forecasting, Victoria, B.C., Canada, September* .
- 521 XIA, H., SHATS, M. & PUNZMANN, H. 2010 Modulation instability and capillary wave turbulence. *EPL* **91**,
522 14002.
- 523 ZAKHAROV, V. E. 1968 Stability of periodic waves of finite amplitude on the surface of a deep fluid. *J. Appl.*
524 *Mech. Tech. Phys.* **9**, 190–194.